JOURNAL OF GEOPHYSICAL RESEARCH, VOL. 111, B09312, doi:10.1029/2005JB003974, 2006

Click Here for Full Article

A thinned lithospheric image of the Tanlu Fault Zone, eastern China: Constructed from wave equation based receiver function migration

Ling Chen,[1] Tianyu Zheng,[1] and Weiwei Xu[1]

Received 3 August 2005; revised 30 March 2006; accepted 25 May 2006; published 22 September 2006.

[1] We apply the newly proposed wave equation-based receiver function poststack migration method to the Northern China Interior Structure Project broadband data to image the lithospheric structure of the Tanlu Fault Zone area in eastern China. Our migration result reveals a 60- to 80-km-thick present-day lithosphere beneath the study region, significantly thinned from the Paleozoic lithosphere of >180 km. The lithosphere-asthenosphere boundary (LAB) is coherently imaged along the ~300-km east-west profile, displaying an arc-like shape with its apex roughly coincident with the transverse location of the Tanlu Fault Zone on the surface. An obvious uplift from ~36 km to ~32 km of the Moho is also clearly detected right below this fault zone. The coincidence of the imaged Moho uplift and the LAB apex with the surface location of the Tanlu Fault Zone provides seismological evidence for the steep geometry and deep penetration of the fault system, and indicates that the Tanlu Fault Zone might have acted as a major channel for anthenosphere upwelling during the Mesozoic-Cenozoic continental extension and lithospheric thinning in eastern China. Frequency analysis and synthetic modeling suggest that both the Moho and the LAB are sharp and strong. The latter, in particular, is constrained to have a 3–7% drop in S wave velocity over a depth range of 10 km or less. Such a rapid velocity change at the base of the lithosphere in the study region cannot be solely explained by thermal variation, but likely reflects the presence of volatiles or melt in the asthenosphere, or is partially attributed to the compositional contrast between the preserved depleted and dehydrated cratonic lithospheric veneer and the uplifted hydrated and fertile asthenospheric materials.

Citation: Chen, L., T. Zheng, and W. Xu (2006), A thinned lithospheric image of the Tanlu Fault Zone, eastern China: Constructed from wave equation based receiver function migration, *J. Geophys. Res.*, *111*, B09312, doi:10.1029/2005JB003974.

1. Introduction

[2] The eastern China continent, a part of one of the oldest cratons on Earth (3.8–2.5 Ga) [*Jahn et al.*, 1987; *Liu et al.*, 1992], has undergone fundamental lithospheric rejuvenation in late Mesozoic and Cenozoic, with the development of large sedimentary basins, high heat flow, extensive seismicity and widespread volcanism [*Griffin et al.*, 1998; *Fan et al.*, 2000; *Xu*, 2001; *Ren et al.*, 2002]. During this period, the thick cratonic lithosphere (>180 km) lost a significant proportion of its deep mantle keel [*Menzies et al.*, 1993; *Griffin et al.*, 1998]. Many hypotheses and models have been put forward to interpret the Mesozoic destabilization and present complex lithospheric structure of the eastern China continent, such as rifting [*Tian et al.*, 1992], delamination [*Gao et al.*, 1998, 2004], thermal and chemical erosion [*Xu*, 1999, 2001], mantle plume [*Deng et al.*, 1998, 2004] and basaltic underplating [*Zhang and Sun*, 2002]. All of these hypotheses are associated with widespread asthenosphere upwelling since late Mesozoic. Preexisting large fault systems and shear zones, such as the Tanlu Fault Zone, the main active strike-slip fault zone in eastern China, are believed to have facilitated the ascending of asthenosphere and played an important role in the Mesozoic-Cenozoic thinning of the cratonic lithosphere [*Xu*, 2001; *Xu et al.*, 2004; *Zheng et al.*, 1998; *Yuan*, 1996]. Geothermal studies, petrologic and isotopic data from Tertiary basalts as well as entrained mantle xenoliths, imply that the Cenozoic lithosphere is thinned to only 70–80 km depth [*Hu et al.*, 2000; *Xu*, 2001; *Xu et al.*, 2004]. Such estimation, however, mostly relies on the spatially confined mantle samples. How well these samples characterize the mantle region is yet unclear. Previous seismic tomography studies have revealed a complex and dramatically thinned lithosphere beneath eastern China [*Chen et al.*, 1991; *Yuan*, 1996; *Zhu et al.*, 2002]. The resolution is, however, rather low due to the confined data coverage and intrinsic limitation of the methods (see below). For localized areas, especially the major fault systems including the Tanlu Fault Zone, improved geophysical observations and high-resolution lithospheric mapping data are required to delineate the lithospheric architecture and to verify various proposed mechanisms for interpretation of the lithospheric process in eastern China [*Xu*, 2001].

[1] Seismological Laboratory, Institute of Geology and Geophysics, Chinese Academy of Sciences, Beijing, China.

Copyright 2006 by the American Geophysical Union.
0148-0227/06/2005JB003974$09.00

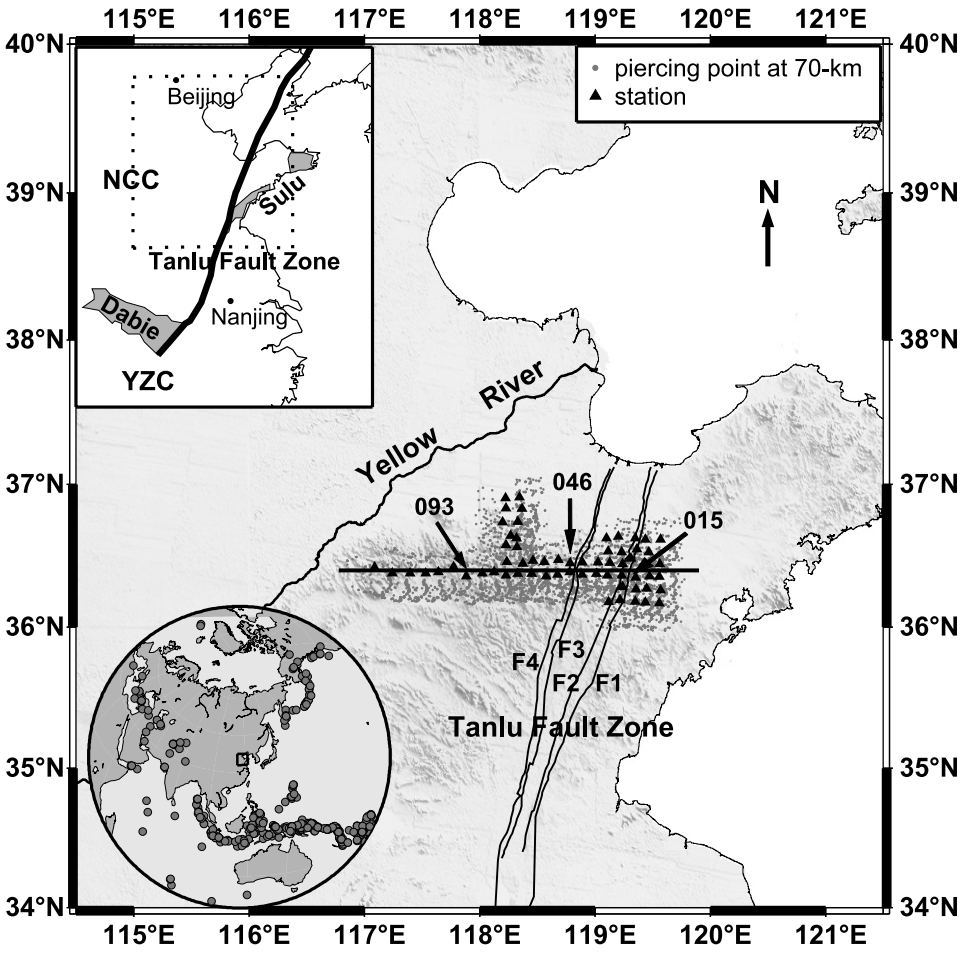

Figure 1. Study region, locations of 62 NCISP broadband seismic stations (triangles), and receiver function imaging profile (thick straight line). The profile traverses all the four constituent faults (F1–F4 from east to west) of the Tanlu Fault Zone. Three stations (093, 046, and 015) are marked, for which the moveout-corrected receiver functions are plotted in Figure 2. Piercing points at 70-km depth for P-to-S converted phases are shown as gray dots. The bottom inset shows the distribution of teleseismic events used, more than 80% of which concentrated within a back-azimuth range of 110–240°. The top inset shows the tectonic setting of the study region in eastern China. Shaded areas are the Dabie-Sulu ultrahigh-pressure metamorphic belt. The Archean North China Craton (NCC) to the north and the Proterozoic Yangtze Craton (YZC) to the south are the two major tectonic blocks in eastern China.

[3] The depth extent of the lithosphere is one of the most important features characterizing the lithospheric structure, and has been the subject of much speculation [e.g., *Kumar et al.*, 2005; *van der Lee*, 2002; *Röhm et al.*, 2000; *Polet and Anderson*, 1995; *Anderson*, 1990]. Unfortunately, high-quality seismic observations about the lithospheric thickness have been scarce. Most available ones come so far from surface wave dispersion measurements and tomography imaging [e.g., *Godey et al.*, 2004; *Baumont et al.*, 2002; *Debayle and Kennett*, 2000; *Woodhouse and Trampert*, 1995]. Surface waves provide depth resolutions of several tens of kilometers that are insufficient to allow identification of a sharp discontinuity, and have even poorer lateral resolutions [*Godey et al.*, 2004]. Teleseismic body wave tomography [e.g., *Montelli et al.*, 2004; *van der Lee*, 2002; *Zhao et al.*, 1994, 1997] can resolve smaller-scale structural features, but suffer from resolution decrease and energy leakage at depths as well as horizontal smearing [*Montelli et al.*, 2004]. It is still a challenging work to image the lithosphere in detail using body waves. The recently developed S receiver function technique has been successfully employed to identify the lithosphere-asthenosphere boundary (LAB) [*Vinnik and Farra*, 2000; *Li et al.*, 2004; *Kumar et al.*, 2005]. This technique, however, has a much lower lateral resolution compared with the commonly used P receiver function method [e.g., *Langston*, 1977; *Owens et al.*, 1987; *Zhu*, 2000; *Poppeliers and Pavlis*; 2003a, 2003b], although it sidesteps the interference of the crustal multiple reverberations with the primary conversions at the shallow part of upper mantle [*Farra and Vinnik*, 2000]. On the other hand, the distinct behaviors of P-to-S (Ps) conversion phase and multiple reflected phases under certain conditions, for example, different variation features of amplitude [*Tian et al.*, 2005] or timing [*Bostock*, 1997; *Rychert et al.*, 2005] with respect to ray parameter (epicentral distance), or contrasting incident angle-dependent features, make it possible to distinguish these two kinds of phases directly using the P receiver function technique. In particular, *Rychert et al.* [2005]

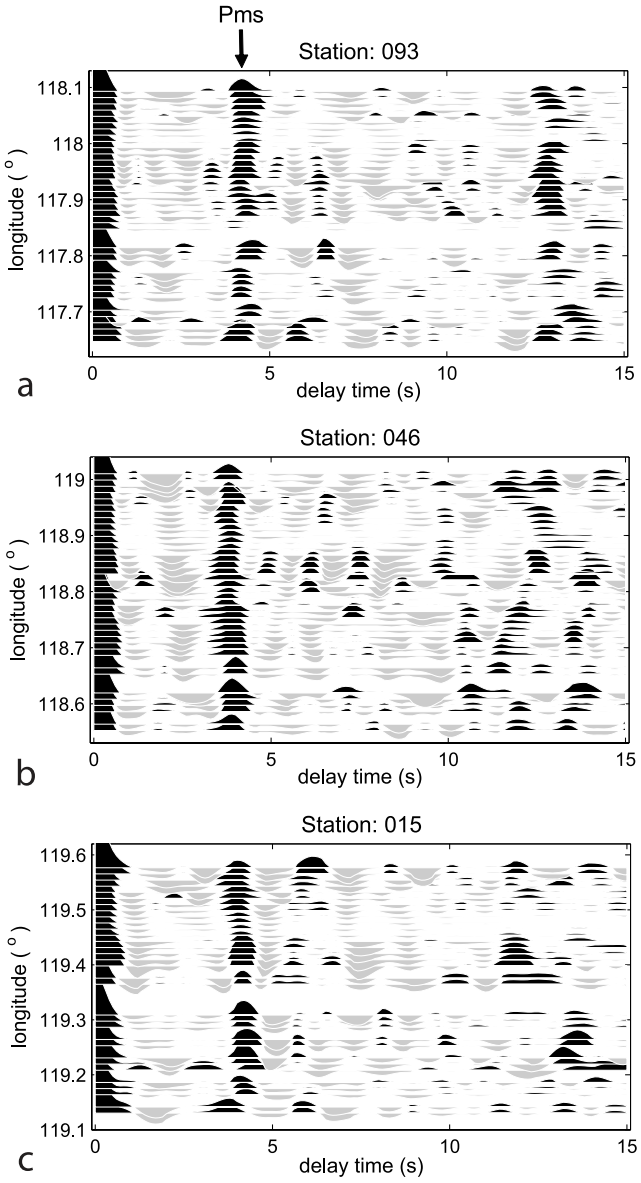

Figure 2. Moveout-corrected receiver functions (0.03–1.0 Hz) at stations (a) 093, (b) 046, and (c) 015 (see Figure 1 for station locations), sorted by the longitude of the piercing points at 70-km depth. Positive polarity energy is plotted in black; negative polarity energy is plotted in gray. Ps phases from the Moho (Pms) are clearly detected at around ~4 s. Strong phases with negative polarities are present in both <4 s and 5–10 s.

showed a good example of P receiver function-based study of the LAB beneath individual stations in eastern North America.

[4] In this study, we use P receiver function data to image the lithospheric structure beneath the Tanlu Fault Zone area in eastern China. The dense stations and therefore dense data coverage (Figure 1) allow us to adopt a newly proposed wave equation based (P) receiver function poststack depth migration (PSDM) method [*Chen et al.*, 2005a, 2005b] to construct simultaneously the lithospheric structural image for a east-west two-dimensional (2-D) profile, instead of the stacking-based analysis for individual stations [e.g., *Rychert et al.*, 2005]. The migration scheme naturally takes into account the effects of diffraction, scattering, and traveltime alternation caused by lateral heterogeneities, and has proven to be particularly useful for recovering complex structural features [*Chen et al.*, 2005a, 2005b]. Considering the difficulty in distinguishing Ps conversions at the shallow upper mantle from intracrustal multiples by accounting for the timing variation with epicentral distance alone, we test the robustness of the LAB image through investigation of image strength variation with P wave incidence angle and varying moveout correction schemes.

[5] We describe the seismic data and the receiver functions processing method in section 2. In section 3, we show the resultant migrated images beneath the Tanlu Fault Zone area, and identify the LAB signal based on image feature analysis and forward synthetic modeling. We further constrain the depth distributions and sharpness of the imaged Moho and LAB in section 4, in the context of lateral variation of seismic velocity, data distribution, frequency contents of data, and waveform comparison. In section 5, we summarize our imaging results and discuss their geophysical implications.

2. Data and Method

[6] Teleseismic data recorded at 62 Northern China Interior Structure Project (NCISP) [*Zheng et al.*, 2005] portable broadband stations (Figure 1) are used in this study for subsurface structural imaging. These stations were emplaced roughly along a west-east direction with average station spacing of about 10 km. The westernmost nine stations operated during a period from December 2001 to February 2003, and the remaining 53 operated from November 2000 to August 2001. Three-component seismograms are selected from 453 events with epicentral distance between 28° and 92°. More than 80% of the events concentrate within a back azimuth range of 110°–240° (inset in Figure 1). Waveforms are windowed from 20 s before and 100 s after the onset of P wave, and receiver functions are constructed using a time domain maximum entropy deconvolution method [*Wu and Zeng*, 1998]. A Gaussian parameter of 5 and a water level of 0.0001 are adopted in the deconvolution. The resultant receiver functions are further band-pass filtered with corner frequencies of 0.03 Hz and 1 Hz to eliminate high-frequency noise. After careful visual inspection, over 5000 receiver functions with high signal-to-noise ratios are selected for further processing.

[7] The delay times of the Ps conversion phases relative to the direct P waves and the piercing points of Ps conversion at depths are calculated according to the one-dimensional (1-D) IASP91 velocity model [*Kennett and Engdahl*, 1991] with modifications for the crustal structure of eastern China (referred to as model EC). The crust in this region is typically thin (<35 km) and slow [*Ma et al.*, 1991; *Gao et al.*, 1998] compared with the global average values. All the receiver functions are then moveout corrected to the case of horizontal slowness $p = 0$. Figure 2 shows examples of the resultant receiver functions at stations 093, 046 and 015 (see Figure 1 for station locations) sorted by the longitude of the piercing points at 70-km depth. Besides the dominant Ps phase from the Moho (~4 s) and its PpPs

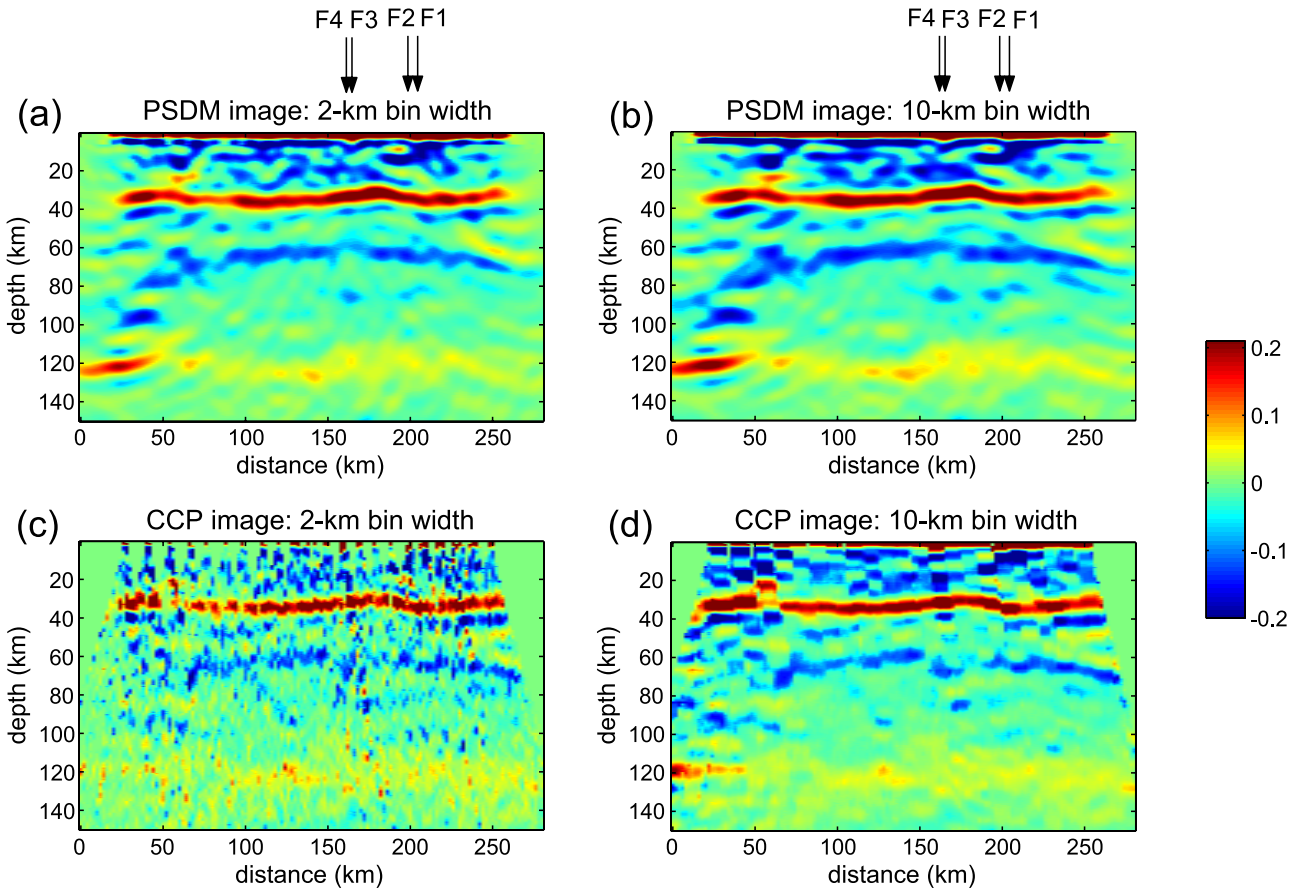

Figure 3. Receiver function images with (a, c) 2-km bin width and (b, d) 10-km bin width used in CCP stacking. Both (a, b) the poststack depth migrated (PSDM) images and (c, d) the CCP depth images are constructed from receiver functions with a frequency range of 0.03–1.0 Hz. Black arrows mark the locations of the four constituent faults (F1–F4) of the Tanlu Fault Zone.

multiples (~14 s), strong phases with negative polarities dominate in both time ranges of <4 s and 5–10 s. The latter could represent either Ps conversions at an upper mantle velocity discontinuity or PpPs multiples from an intracrustal interface. In both cases, negative velocity gradients are required for the associated structure. We will show from their amplitude variation that these phases reflect a true upper mantle structure, likely the LAB of the study region.

[8] According to the coverage of piercing points (e.g., those at 70-km depth shown as gray dots in Figure 1), we construct the subsurface structural image for an east-west profile that intersects the Tanlu Fault Zone at its eastern part (Figure 1). Following the migration procedure described by *Chen et al.* [2005a], the receiver functions are processed with time domain common conversion point (CCP) stacking and subsequent frequency domain poststack depth migration. Rectangular bins with a fixed length of 100-km perpendicular to the profile are used during the CCP stacking process. The bin width parallel to the profile is either fixed or allowed to vary with the data coverage, for later image comparison and robustness assessment of the revealed structural features. The minimum receiver function number in each bin is set to be 20–50, depending on the data density and the depth of the target structure. If not specified, the migrated images shown in the following sections are obtained by adopting the same 1-D velocity model used in calculation of delay times and piercing point locations, and superposing the migrated frequency contents of the stacked receiver functions in a frequency band of 0.03–1 Hz.

3. Lithospheric Image Beneath the Tanlu Fault Zone Area

3.1. General Image Feature

[9] To reveal fine-scale subsurface structural features, especially the geometry of the Moho and possible upper mantle discontinuities, first we use small bin widths of no more than 10 km for most parts of the profile in CCP stacking of receiver functions. Figures 3a and 3b shows the migrated images (hereafter called PSDM images) with two fixed bin widths: 2 km and 10 km (except at edges where gradually widened bins are adopted to compensate reduced number of data), respectively. The two PSDM images essentially reveal similar structural features, despite their large disparity in bin size and therefore suffering different smoothing effects in receiver function stacking. Along the profile, the Moho is clearly identified as a strong positive conversion phase at 30–40 km depths. It presents an obvious uplift with the largest offset right beneath the Tanlu Fault Zone. Signals with negative polarities are dominant both above and below

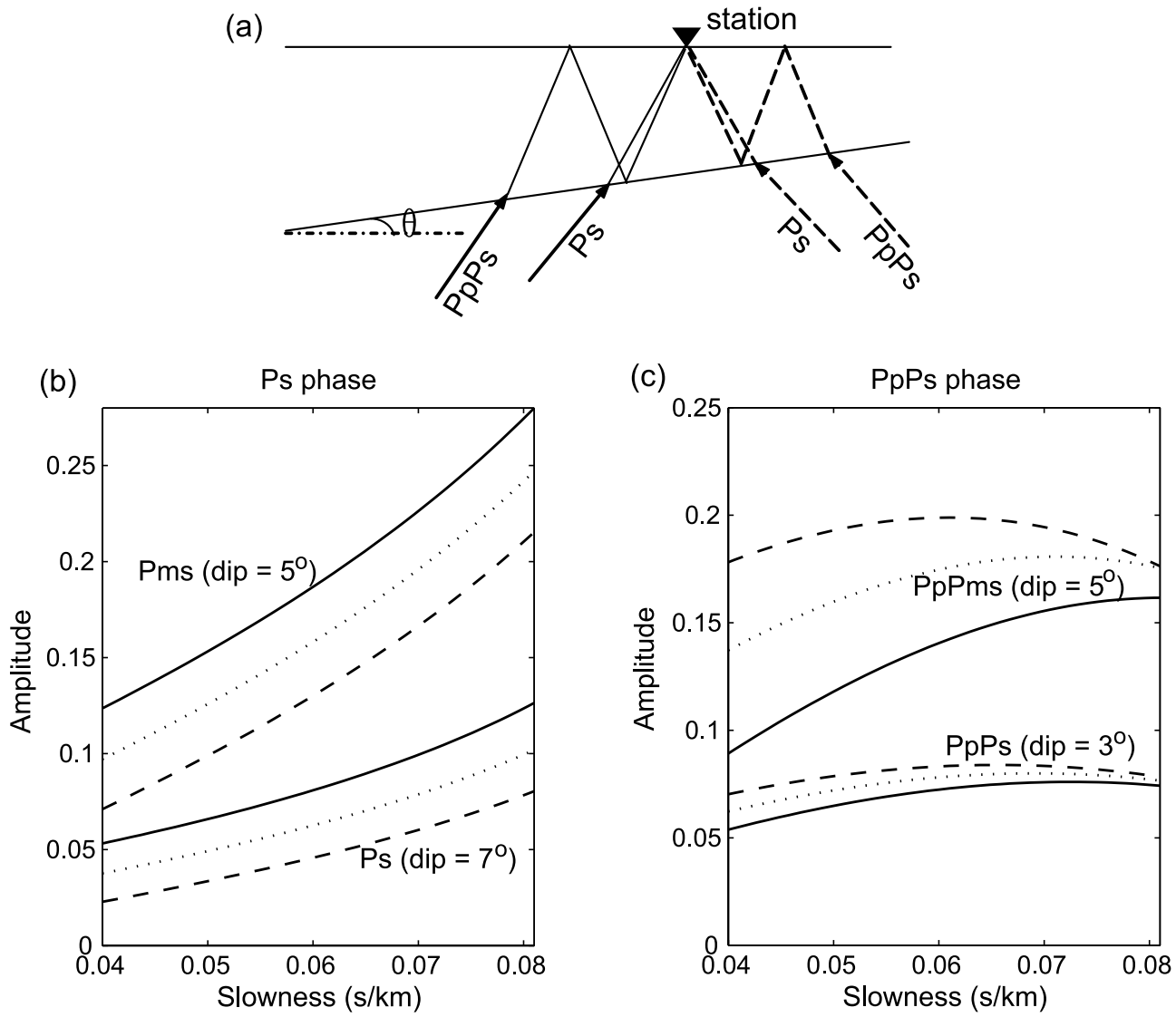

Figure 4. (a) A simple dipping discontinuity model and amplitude variations of (b) Ps conversion phase and (c) PpPs multiples with different incident directions of P waves. Pms and PpPms resemble the phases from a strong discontinuity like Moho with a dip of 5°. Ps produced from an interface with a dip of 7° is used to simulate the Ps conversion at an upper mantle discontinuity, and PpPs from a discontinuity with a smaller dip (3°) is used to simulate intracrustal multiples. Dotted lines represent the dip = 0° (horizontal discontinuity) case, and solid and dashed lines stand for incident directions along and opposite to the inclination of the discontinuity, respectively.

the Moho discontinuity. The intracrustal signals appear cluttered and intermittent, and no discontinuity can be coherently identified along the whole profile. In contrast, a strong mantle phase is continuously detected at 60–80 km depths, exhibiting an arc-like geometry.

[10] A similar curved Moho and an arc-shaped negative mantle phase are also revealed using the more common CCP depth imaging method [*Zhu*, 2000] with the same stacking bin sizes (Figures 3c and 3d), although the signal-to-noise ratios are low and mosaic artifacts are obvious in the CCP images compared with their PSDM counterparts (Figures 3a and 3b). The different image qualities stem from different capabilities of the two imaging methods in handling scattering and diffraction energies caused by lateral heterogeneities [*Chen et al.*, 2005a, 2005b; *Ryberg and Weber*, 2000; *Sheehan et al.*, 2000]. The common image features, however, indicate that both the structural feature of the Moho and the appearance of the strong negative phase below the Moho are robust, irrespective of the imaging method used.

3.2. Lithosphere-Asthenosphere Boundary

[11] The strong arc-shaped phase with negative polarity presented at 60–80 km depth in Figure 3 may either represent the Ps conversion from a real upper mantle discontinuity or result as an artificial image of PpPs multiples from a shallower crustal structure. In either case, the associated discontinuity should be nonhorizontal. This, along with the shallow depth distribution in the upper mantle, makes it difficult to distinguish between these two interpretations either based on the delay time variation with slowness

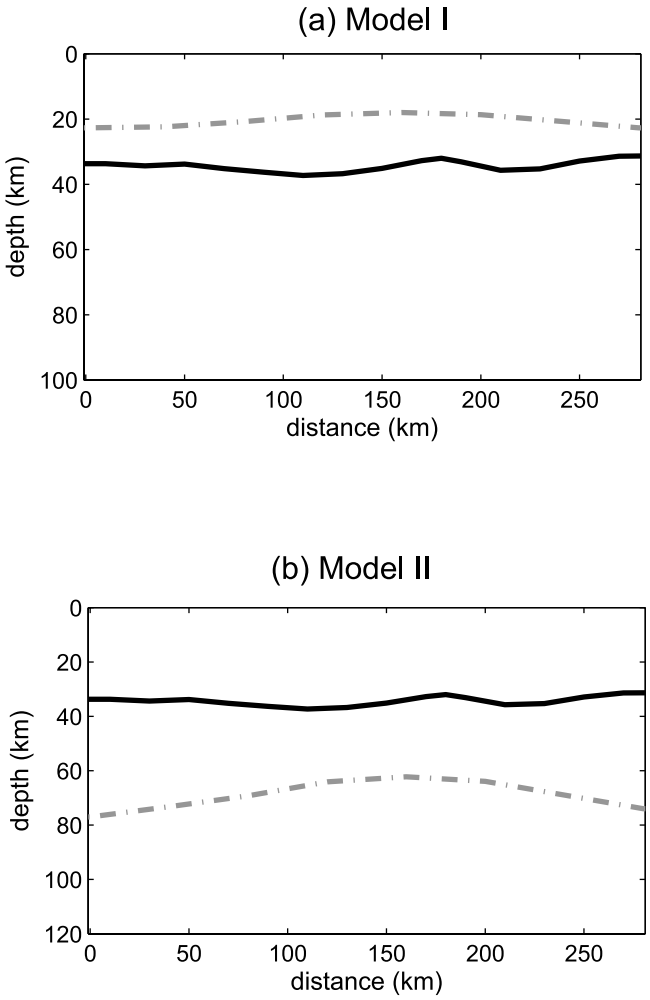

Figure 5. Two synthetic models. Black solid lines mark the Moho, and gray dashed lines denote discontinuities with negative velocity gradients.

[e.g., *Bostock*, 1997; *Rychert et al.*, 2005] or using techniques valid mainly for horizontally layered structures, such as that recently proposed by *Tian et al.* [2005].

[12] On the other hand, distinct behaviors of converted and topside reflected phases upon different incident directions of P waves for a dipping discontinuity (Figure 4) would be helpful for determining the nature of the phase presented in the real data images. Theoretical calculations show that the P waves directed along the inclination of the dipping structure tend to produce stronger Ps conversions, whereas those from the opposite side result in much weaker conversions (solid and dashed lines, respectively, in Figures 4a and 4b). A PpPs multiple, however, exhibits different amplitude variations with respect to the incident directions. It is considerably enhanced when the P waves strike the discontinuity more close to the normal incidence case (perpendicular to the inclination of the discontinuity) and much weakened otherwise (Figure 4c). Such contrasting features are true for dipping structures with both positive and negative velocity gradients and would lead to different slowness-integrated image strengths of Ps conversion and PpPs multiples using separate back azimuth sets of data.

[13] To attain a straightforward image comparison, we reproduce the PSDM images with two subsets of the data in nonoverlapping back azimuth ranges: 0–180° and 180°–360°, respectively. All the 963 receiver functions in the second subset and randomly selected 963 out of 4279 receiver functions in the first subset, having comparable data density and coverage with each other, are used both separately and jointly in imaging. For better comparison, we also perform synthetic modeling with two simple models (Figure 5). Model I contains an arcuate discontinuity with a negative velocity gradient (4% for P wave and 5.5% for S wave) in the middle crust (Figure 5a); model II comprises a similar discontinuity but emplaced at 60–80 km depths in the upper mantle with an enhanced magnitude of undulation (Figure 5b). In addition, an undulating crust-mantle interface similar to the Moho revealed in the data images (Figure 3) is also built into both models. Synthetic seismograms are calculated by a 2-D hybrid method [*Wen and Helmberger*, 1998] and receiver functions are constructed in the same manner as that for the real data set. The receiver functions used in imaging are picked such that the data coverage and density in the cases of left-, right-, and two-sided incidence of P waves resemble those of the real data in the back azimuth ranges of 180°–360°, 0–180°, and both, respectively (Figure 6e).

[14] Comparisons of the data images (Figure 6, left) with their synthetic counterparts (Figures 6, middle, and 6, right) indicate that the strong negative phase coherently observed around 70-km depth (Figures 3 and 6, left) likely represents a real structure in the upper mantle. This conclusion is reached based on the following three observations that show large disparities of the target phase from crustal PpPs multiples but close similarities to the true Ps conversions.

[15] 1. For rays coming from west (back azimuths within 180–360°), the west downdipping part is clearly identified, but the east downdipping part appear weak, even invisible in the image (Figure 6a, left). Using the subset of data from east (0–180°), on the other hand, the former weakens, while the latter becomes more predominant (Figure 6b, left). Such a variation in image strength with incident direction of P waves is also observed in the image of the upper mantle discontinuity in model II (Figures 6a, right, and 6b, right) and consistent with the theoretical predictions for Ps phases (Figures 4b). It is, however, obviously different from the artificial image induced by the crustal PpPs multiples in model I (Figures 6a, middle, and 6b, middle) which is affected by the coming direction of data in an opposite way (Figure 4c).

[16] 2. Including both sets of data in imaging, the target phase in the image (Figure 6c, left) and the synthetics (Figure 6c, right) shows smoother strength variation along the profile, and roughly maintains its arcuate geometry for the single-side-incidence images (Figures 6a, left; b, left; 6a, right; and b, right). On the contrary, the crustal PpPs-induced artificial image is significantly weakened, blurred, and becomes intermittent with an apparently reduced slope (Figure 6c, middle).

[17] 3. With moveout corrections based on PpPs delay times instead of Ps delay times as usually done for receiver functions, the image strength of the upper mantle discontinuity is considerably reduced, especially at both edges of the profile (Figure 6d, right), as is the image of the target negative

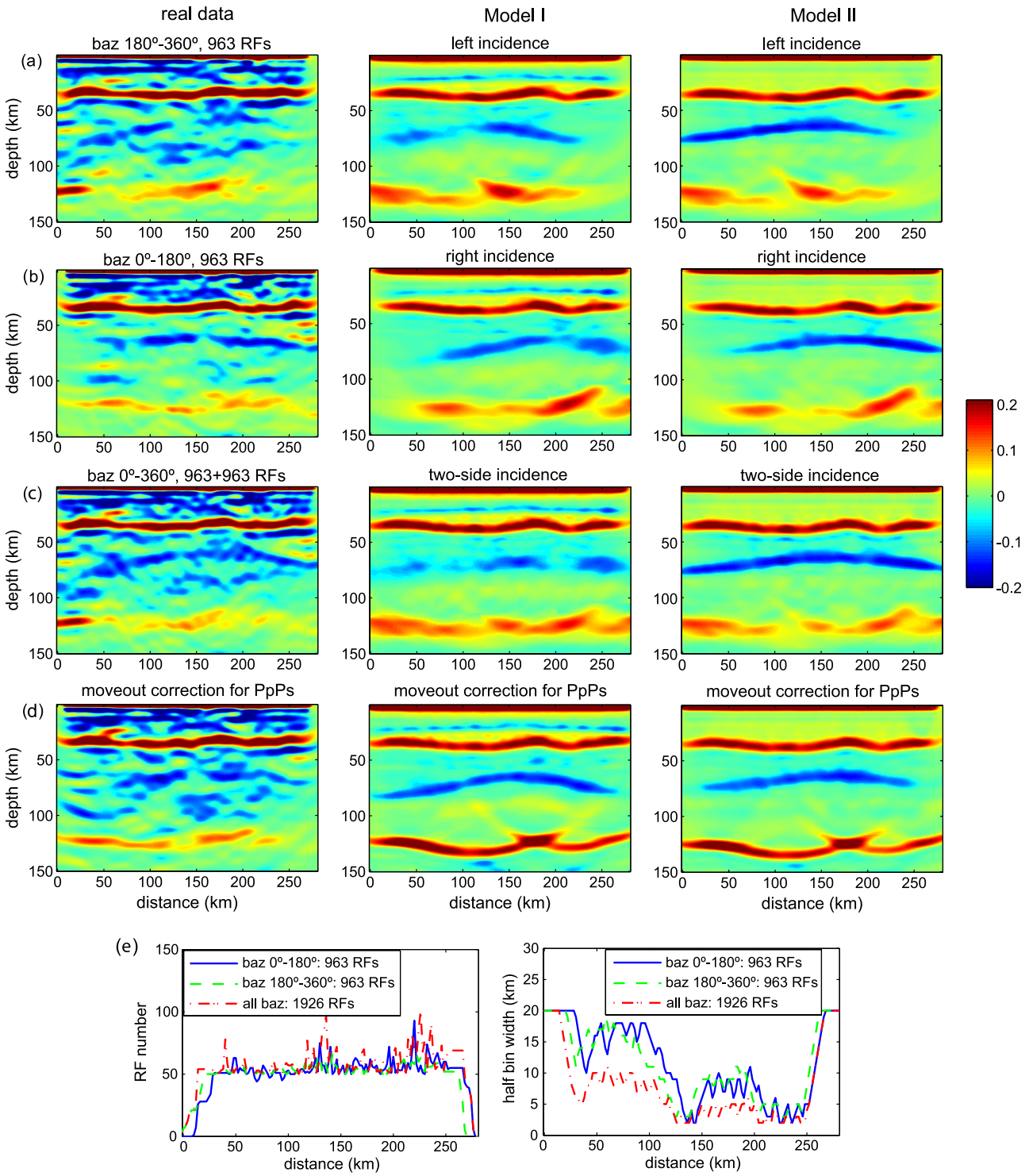

Figure 6. PSDM images constructed from different subsets of (left) real data and (middle, right) synthetic data for the two models shown in Figure 5. (e) (left) Numbers of receiver function in the bins and (right) bin widths used in CCP stacking at 50-km depth.

phase in the real data (Figure 6d, left). By contrast, the PpPs artificial image is significantly enhanced with the correct moveout corrections (Figure 6d, middle). These observations suggest that the strong negative phase at ~70-km depth in the data image more likely reflect Ps conversions from a real upper mantle discontinuity beneath the study region.

[18] Another piece of evidence for the Ps conversion nature of the strong negative phase comes from identification of possible PpPs multiples from a same discontinuity (Figure 7). By performing moveout correction based on the delay times of PpPs over a discontinuity at 70-km depth and including all the data in migration, an arc-shaped image

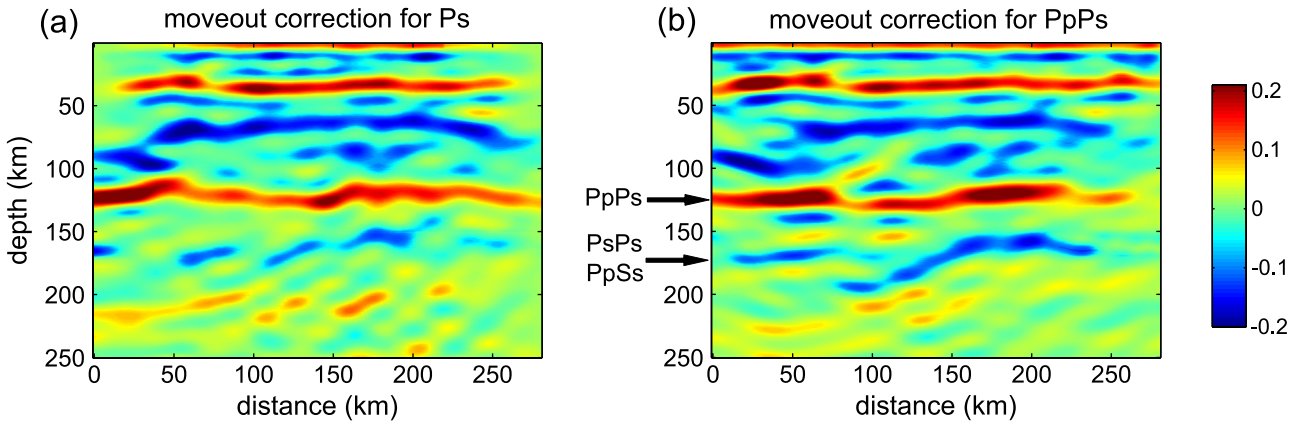

Figure 7. PSDM images with moveout correction (a) for Ps phases and (b) for PpPs phases from a discontinuity at 70-km depth. Both images are constructed from all the receiver functions with a frequency range of 0.03–0.6 Hz, and using same migration velocities so that the depth distributions in Figures 7a and 7b are comparable. Parameters for CCP binning are same as those used in Figure 3b. The image strength is multiplied by the square root of the depth at each point to enhance the deeper part of the image. Predicted depths of Moho multiples are marked by black arrows. For both the Moho multiples and the arc-shaped signal at 160–200 km depth, the relatively weak and blurred image at the eastern edge of the profile is largely attributed to the uneven distribution and limited coverage of data.

with negative polarity is clearly presented in the depth range of 160–200 km (Figure 7b). In contrast, such an image is weak and nearly invisible with moveout correction for Ps phases (Figure 7a), suggesting that it is possibly a topside multiple-induced artifact. Note that relatively lower frequency contents of data (0.03–0.6 Hz) are considered here for better imaging at larger depths. The arc-shaped image is apparently not associated with the PsPs + PpSs multiples of

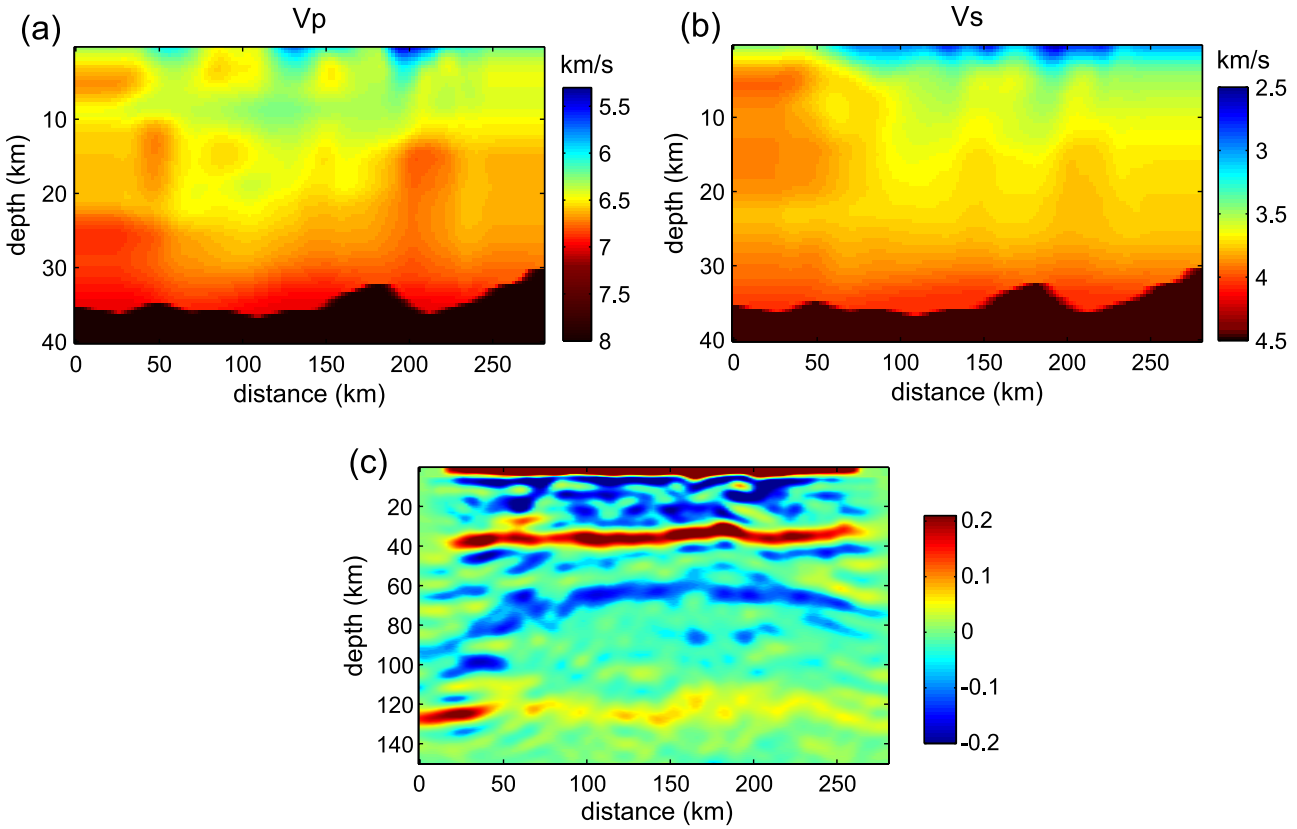

Figure 8. A 2-D crustal model of (a) P wave velocity and (b) S wave velocity constructed on the basis of receiver function inversion for individual stations (T. Zheng et al., manuscript in preparation, 2006) and superposed with a curved Moho similar to that shown in Figure 3; (c) PSDM image using the velocity models in Figures 8a and 8b with the same CCP binning parameters used in Figure 3b.

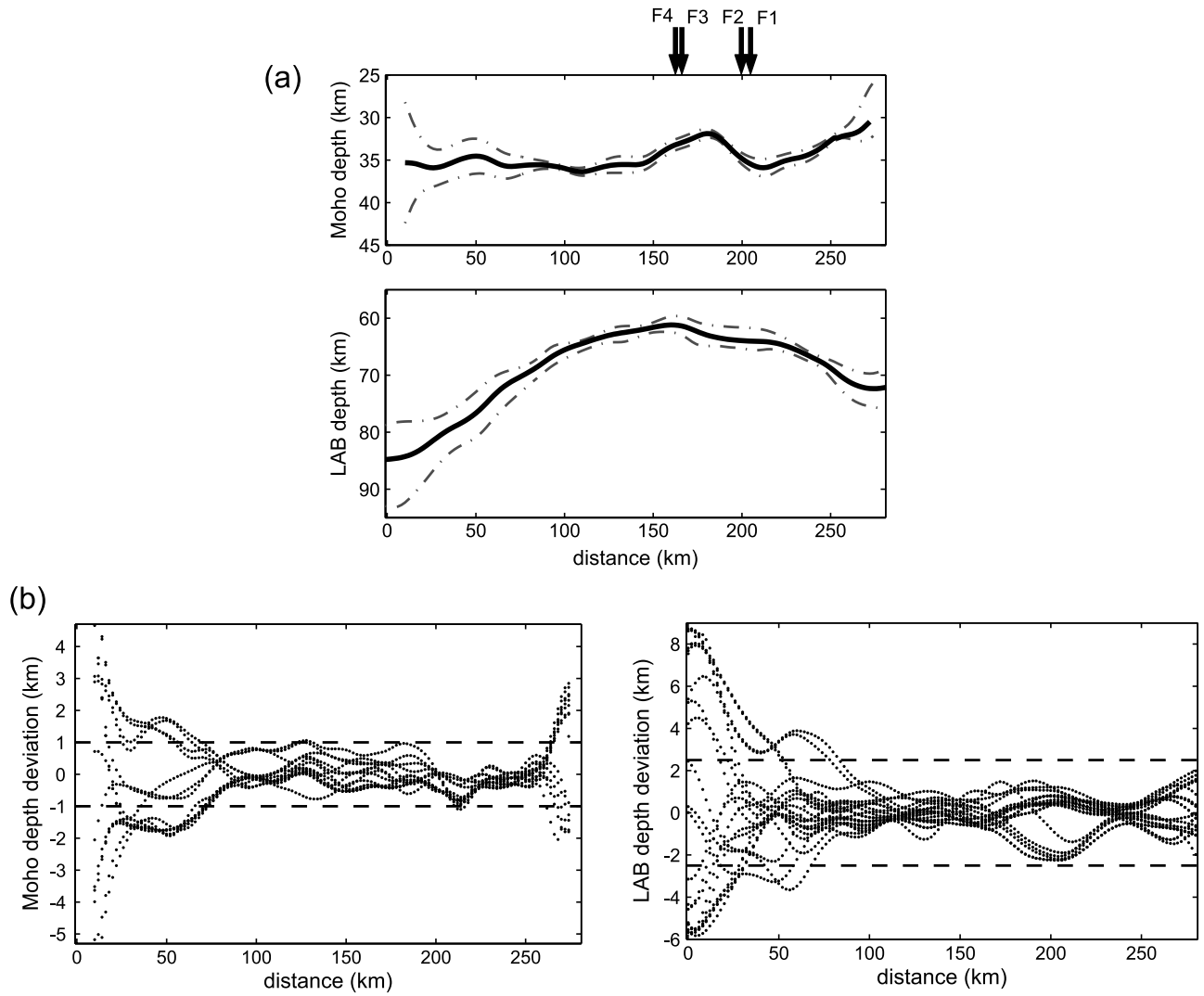

Figure 9. (a) Estimated depth distributions of the imaged Moho and LAB and (b) their depth deviations from different velocity models, CCP binning schemes, and subsets of data. Solid lines and dashed lines in Figure 9a represent the mean depth distributions, the shallowest and deepest depths estimated for the Moho and the LAB, respectively. The four constituent faults (F1–F4) of the Tanlu Fault Zone are also marked in Figure 9a. Dashed lines in Figure 9b mark the ±1-km depth deviations of the Moho and the ±2.5-km depth deviations of the LAB, respectively.

the Moho because of its significant undulation and larger depths, although it interferes with these phases at ~160-km depth. Moreover, its depth distribution and arc-like geometry are all consistent with those predicted for the PpPs multiples from an arcuate upper mantle discontinuity similar as that appears at 60–80 km depth in the data images (Figure 3). These observations further confirm that this deeper signal and the strong arc-like image in the shallow mantle likely represent the PpPs and Ps pairs of a real velocity discontinuity.

[19] The data analysis and synthetic modeling provide evidence for a real upper mantle discontinuity within a depth range of 60–80 km beneath the study region. By virtue of its negative polarity, continuity and coherency, and its depth distribution, we speculate that this discontinuity represents the LAB of the region. It uplifts right beneath the Tanlu Fault Zone and extends downward to both west and east with a depth variation up to 15–20 km.

[20] Also note that in addition to the strong LAB Ps phase in the upper mantle, some negative signals appear sporadically in the data image, mostly below the LAB (Figure 6, left). The strongest ones are observed when only utilizing signals coming from west (180–360°) (Figure 6a, left). Owing to the relative high dispersion of the back azimuths in this case (insert in Figure 1), small-scale heterogeneities could result in less coherent stacking of data along the profile, and consequently lead to ineffective noise suppression in the images. These signals may either be crustal reverberations or represent true Ps conversion or scattering associated with small-scale heterogeneities in the upper mantle. It is,

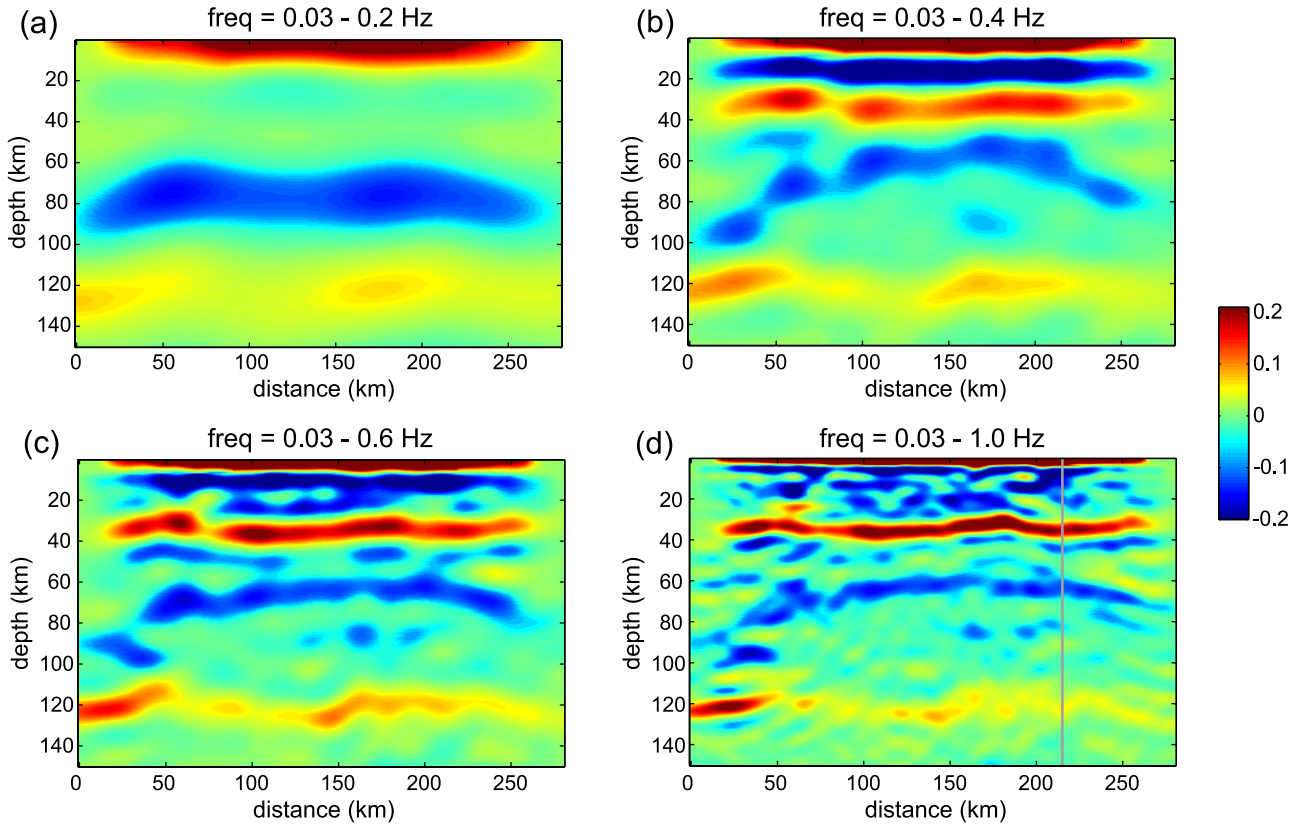

Figure 10. PSDM images obtained by using different frequency contributions of receiver functions for (a) 0.03–0.2 Hz; (b) 0.03–0.4 Hz; (c) 0.03–0.6 Hz; and (d) 0.03–1 Hz. Parameters adopted in CCP stacking are same as those used in Figure 3b. Gray line in Figure 10d marks the trace location for waveform comparison shown in Figure 11.

however, hard to arrive at a definitive conclusion based on receiver function observation alone.

4. Constraints on the Seismic Properties of the Moho and the LAB

[21] We further explore the seismic properties of the Moho and the LAB of the study region. We investigate the influences of lateral variation of seismic velocity and data distribution using various 2-D models, different CCP binning schemes and different subsets of data, and estimate the depth variations of the imaged Moho and LAB in a statistical manner. We perform frequency analysis and forward waveform modeling to constrain the sharpness of the discontinuities, especially the LAB.

4.1. Depth Variations

[22] The depth distributions of the imaged Moho and LAB are prone to be affected by many factors, including the migration velocity model, the CCP binning schemes and the subsets of data used in migration. The velocity model is likely the most dominant among these factors. We have used the 1-D model EC to construct the PSDM images for the study region. This model represents the average subsurface structure of the eastern China continent. To investigate the influence of lateral heterogeneity in the crust on the PSDM image, we incorporate various available 2-D crustal models with model EC in migration. Some 2-D models come from previous deep seismic exploration studies [*Wang et al.*, 2000; *Zhang and Tang*, 1988] and seismic tomography [*Yuan*, 1996] for the same area or nearby regions. The latest crustal model used here is derived from receiver function inversion for individual stations (T. Zheng et al., manuscript in preparation, 2006). Moreover, the topography of the Moho is also taken into account in designing the models. Figure 8 shows an example of the 2-D P wave velocity (Vp) and S wave velocity (Vs) model for the top 40 km and the corresponding PSDM image with the same CCP binning as used in Figure 3b. The 2-D model-based images display similar features as those presented in the images using the 1-D model EC (compare Figure 8c with Figure 3b). We also test various Vp/Vs ratios from 1.78 to 1.85 for the uppermost mantle above the LAB. We find that varying the mantle Vp/Vs ratios within this range do not significantly affect the shape of the LAB image. In addition, alternative CCP binning schemes, including setting different lower and upper thresholds for bin widths, and numerous randomly selected subsets of data (within back azimuth ranges similar to those for Figure 6 (left)) are also employed in separate migration processes (with either the 1-D velocity model or various 2-D models), to investigate the possible influence of stacking and data distributions on the migrated images. Little difference is detected between the resultant images (not shown) and those presented in Figures 3, 6 (left), and 8c.

[23] Our results indicate that the imaged structural features on the whole are not notably affected by using different

Table 1. Model Parameters in Synthetic Modeling

	Parameters	
Discontinuity	Vs Contrast, %	Depth Range, km
	Lab	
1.7 s		
First step	2, 5, 8	0, 5, 10, 15
Second step	3, 4, 5, 6	2, 3, 4, 5, 6, 7
Third step	3.5–5.5, every 0.5	3, 4, 5, 6
1.2 s	4–7.5, every 0.5	4–11, every 1
2.2 s	2.5–4.5, every 0.5	0–5, every 1
	Moho	
1.7 s	6, 8, 10, 12, 15.6	0, 1, 3, 5, 10
1.2 s, 2.2 s	10, 12, 14	0, 1, 3

velocity models, various CCP binning schemes and different subsets of data as well. The estimated depth distributions of the Moho and the LAB (determined at the maximum amplitudes of the image) with reasonable velocity models and stacking parameters are robust in the sense that the maximum depth variations are less than 2 km and 5 km for the former and the latter, respectively, in most parts of the profile (Figure 9). The scarcity and high dispersion of data coming from west is likely responsible for the large uncertainties at the western end of the profile (Figure 9b).

4.2. Sharpness

[24] The sharpness of a seismic discontinuity can be described by the velocity contrast at the discontinuity and the depth range over which the velocity contrast occurs. Next we provide constraints on the sharpness of the Moho and the LAB through frequency analysis and waveform modeling.

[25] In section 4.1, all the PSDM images except Figure 7 are produced with the cutoff frequencies of 0.03 and 1 Hz that are also used for band-pass filtering of the raw receiver functions. Both the Moho and the LAB are clearly imaged upon this frequency band. With gradually lowered frequency contents considered in imaging, the Moho is markedly smoothed and weakened, and becomes undetectable with cutoff frequencies below 0.2 Hz (Figures 10a–10c). This is also true for the LAB. In particular, for the images with frequencies lower than 0.6 Hz, the side lobes of the Moho Ps conversion phase as well as the possible crustal multiples significantly interfere with the Ps phase of the LAB, making it an ambiguous feature (Figures 10a and 10b). Using higher cutoff frequencies in band-pass filtering of the raw receiver functions and subsequent imaging cannot improve the resolution noticeably for both the Moho and the LAB but result in apparently lowered signal-to-noise ratios in the images. In this respect, the frequency dependence of the PSDM image (Figure 10) suggests that the cutoff frequency of 1 Hz is the most appropriate for imaging the lithospheric structure of the study region. The fact that the Moho and the LAB are best imaged by involving frequencies as high as 1 Hz indicate that for the study region, both the crust-mantle and the lithosphere-asthenosphere transitions are rather sharp and occur over depth intervals comparable to the half wavelengths of the incoming P waves at the corresponding depths [*Bostock*, 1999].

[26] We further constrain the sharpness of the discontinuities, especially the LAB through forward waveform modeling based on model II (Figure 5b). Waveforms converted at the LAB depend on not only the sharpness of the discontinuity but also the absolute depth and topography of the discontinuity, and the dominant period of the incident P wave [*Rychert et al.*, 2005; *van der Meijde et al.*, 2003]. The estimated depth distributions of the Moho and the LAB (Figure 9a) are adopted in synthetic calculation as the limits of the possible variation in the other parameters. In these models, the frequency-dependent image (Figure 10) restricts the depth intervals in our modeling to 0–10 and 0–15 km, respectively, for the Moho and the LAB. Unlike many receiver function studies that used 1-D model-based waveform inversion techniques for individual stations [e.g., *Rychert et al.*, 2005; *Zheng et al.*, 2005], we simultaneously generate synthetics along the whole profile by the 2-D hybrid method [*Wen and Helmberger*, 1998] that naturally takes into account the effect of topography on the waveforms. Synthetics that match the slowness and back azimuth of each of the real waveforms are selected for waveform comparison. To account for amplitude variations with respect to back azimuth, we stack the synthetics coming from east and west separately and jointly in each bin and perform waveform comparison with their real data counterparts, similar as we have done in Figure 6. To account for the influence of dominant period of incident P waves on the waveform of Ps converted phase, we adopt three values of 1.2 s, 1.7 s and 2.2 s individually in our synthetic calculation, given that most of the direct P waves in our data have dominant periods falling within 1.2–2.2 s.

[27] Different velocity contrasts and depth intervals are tested for the LAB and the Moho as well (Table 1) with each dominant period of incident P waves. The computation expense of the synthetic method used does not allow us to test too many models, and therefore limits the resolutions of our study to be ~0.5% and 1 km for the velocity drop and depth range, respectively. It is, however, sufficient to provide first-order constraints on the seismic properties of the LAB beneath the study region. Our modeling results suggest that the crustal velocity structure appears to have minor effects on the velocity drop estimation of the LAB; in particular, variations in velocity gradient up to ~50% over the Moho (from 10% to 15.6%) do not significantly affect the waveform of the Ps phase at the LAB (compare purple line and black line in Figure 11a). Comparison of the real receiver functions with the synthetics at various transverse locations suggests that with the dominant P wave period of 1.7 s, a depth range of 10 km is apparently too large to produce the observed Ps conversions at the LAB, yet velocity drops within a range of 3.5–5.0% over 3–6 km fits the real data reasonably well at most of the locations along the profile (see Figures 11a and 11b, for example). Considering a longer period of incident P waves (2.2 s), the estimated velocity drops reduce to 3.0–4.0% occurring over a narrower depth range of 0–4 km. By way of contrast, decreasing the dominant period of P waves to 1.2 s increases the allowable depth range to 5–10 km and also enlarges the allowed velocity contrasts to 5.0–7.0% (Figure 11c). The velocity increase at the Moho, however, cannot be strictly constrained due to the simple crustal model adopted in our synthetic modeling. Nevertheless, general waveform comparisons within the dominant period range of incident P waves suggest that the Moho of the study region is sharp (likely $\leq$ 3 km,

Figure 11a), in agreement with the frequency-dependent feature of the migrated image (Figure 10).

5. Interpretation and Discussion

[28] Lithospheric reactivation and thinning have long been proposed as the dominant process occurred in eastern China during late Mesozoic and Cenozoic, yet direct seismic observations of fine-scale lithospheric structures have been scarce. By applying the newly proposed wave equation based receiver function migration technique to recently collected high-quality broadband seismic data, we are able to image the lithospheric structure beneath the Tanlu Fault Zone area in detail.

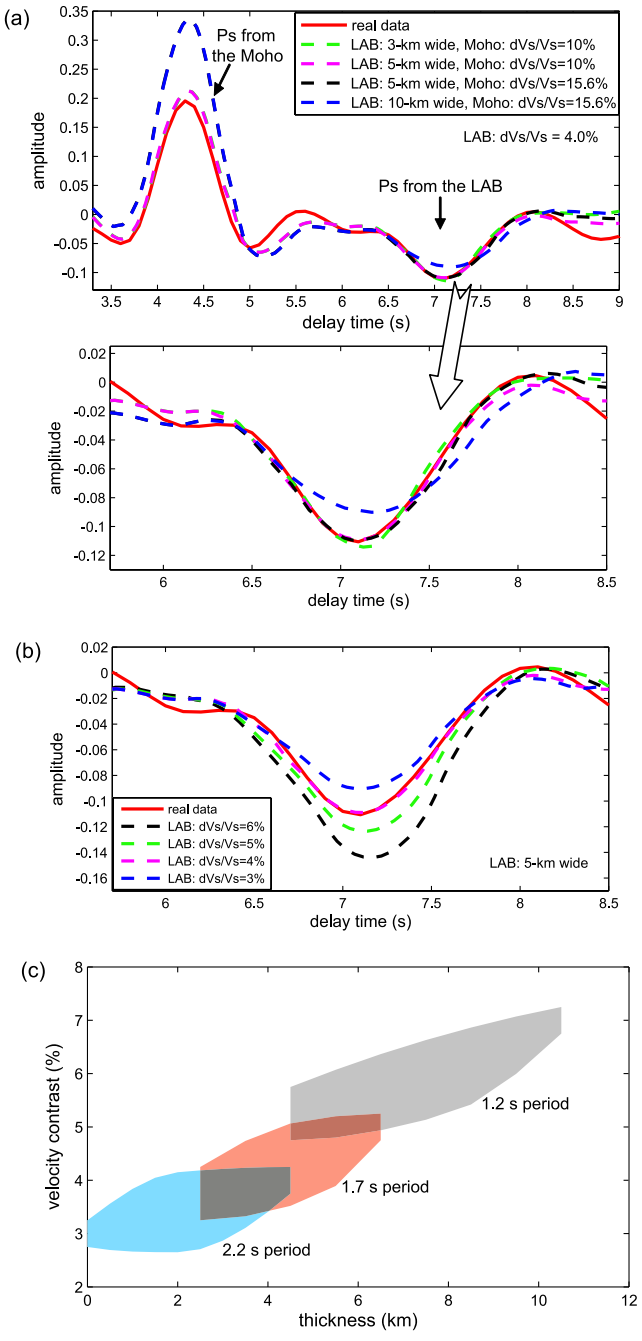

[29] Substantial lateral heterogeneities are markedly presented in the whole lithosphere range. The crustal image is rather complicated, and dominated by strong signals of negative polarity. This feature might reflect widespread velocity reversals and considerable structural complexity in the crust, and is probably associated with significant Mesozoic-Cenozoic lithospheric destruction and voluminous magmatism occurred in eastern China [*Deng*, 1988; *Liu*, 1992; *Ren et al.*, 2002]. The Moho, by way of contrast, appears continuous and sharp, likely indicating the presence of a rapid crust-mantle transition beneath the study region [*Xu et al.*, 1995]. Despite its average depth of 34 km, which is in fairly good agreement with seismic tomographic results [*Chen et al.*, 1991; *Yuan*, 1996], small-scale undulations, especially an obvious uplift of the Moho from ~36 km to ~32 km right below the Tanlu Fault Zone is clearly detected in our PSDM images. The coincidence of the Moho uplift with the surface location of the Tanlu Fault Zone (Figures 3b and 9a) provides evidence for its steep geometry and deep penetration into the lithospheric mantle [*Zheng et al.*, 1998, 2001].

[30] More interestingly, the LAB beneath the study region is coherently identified in our PSDM images. The average depth of ~70 km of the LAB corroborates well with seismological observations [*Chen et al.*, 1991; *Zhu et al.*, 2002; *Huang et al.*, 2003] as well as geochemical, geothermal and petrographic data [*Fan et al.*, 2000; *Xu*, 2001; *Xu et al.*, 2004] that indicate a present-day lithosphere of 60–80 km in eastern China. However, none of these studies reveal a detailed depth variation and seismic features of the LAB beneath the Tanlu Fault Zone area. For example, previous seismic tomographic images mentioned above have lateral resolutions of 200–400 km, which does not allow to identify

Figure 11. (a, b) An example of waveform comparisons between the real receiver functions (solid red lines) and synthetics (dashed lines) at a transverse location marked in Figure 10d. In all the cases shown here, synthetic modeling is performed with a dominant period of incident P waves of 1.7 s and the models are set either with a fixed velocity contrast (4.0%) but occurring over different depth intervals (Figure 11a) or with a fixed depth interval (5 km) but different velocity contrasts (Figure 11b) at the LAB. The Moho is designed as a 3-km-thick transition zone with a S velocity decrease either of 10% (green and purple lines in Figure 11a and all those in Figure 11b) or similar to that given in PREM (15.6% [*Dziewonski and Anderson*, 1981]) (black and blue lines in Figure 11a). Both real data and synthetics are resulted from time domain CCP stacking of the 0.03- to 1-Hz band-pass-filtered receiver functions within 10-km-wide bins. At this location an S velocity drop of 4.0 ± 0.25% occurring over 5 ± 0.5 km at the LAB gives the best fit to the real data. With increased (2.2 s) and decreased (1.2 s) dominant periods of incident P waves, the LAB can be modeled with 3.5 ± 0.25% velocity drop over 3 ± 0.5 km and 5.5 ± 0.25% over 8 ± 0.5 km, respectively (with similar misfit to the data as that of the purple line show in Figures 11a and 11b). In all the cases, the velocity increases at the Moho appear to less than 15.6% and occur over a depth range of ≤3 km. (c) Model constraints of the LAB along the whole profile at the three dominant periods of incident P waves.

any smaller-scale structural feature of the LAB. Our images, on the other hand, show clearly an arc-shaped LAB resting at ~60–80 km depths with its apex roughly coincident with the transverse location of the Moho uplift, and hence that of the Tanlu Fault Zone at the surface. The LAB deepens away from its apex, especially to the west, with a maximum depth variation of ~20 km (Figure 9a). The geometry and depth distributions of the imaged LAB and the Moho as well are consistent with previous speculation that the deeply persisting Tanlu Fault Zone facilitated the upwelling of hot anthenosphere materials accompanying the continental extension and lithospheric thinning in eastern China during the late Mesozoic-Cenozoic time [*Yuan*, 1996; *Zheng et al.*, 2001; *Xu*, 2001].

[31] In addition to the shallow depth of the imaged LAB, which confirms the occurrence of significant removal of ancient lithospheric mantle keel beneath eastern China [*Xu*, 2001; *Griffin et al.*, 1998; *Fan and Menzies*, 1992], the retrieved structural feature of the lithosphere provides seismological constraints on the thermal and compositional state of the upper mantle and lithospheric architecture in the study region. The LAB appears relatively sharp (≤10 km) and strong (S wave velocity contrast 3–7%), indicating the presence of a sharp velocity gradient at the base of the lithosphere. Several factors, including temperature, phase changes, and compositional variations, might contribute to such a rapid change in seismic property of the continental lithosphere.

[32] First, it is well established that in the upper mantle, seismic velocities are mostly sensitive to temperature [*Godey et al.*, 2004; *Deschamps et al.*, 2002; *Goes et al.*, 2000; *Duffy and Anderson*, 1989]. If the distinct S wave velocity drop at the LAB is purely thermal origin, then a rapid increase in temperature gradient (>20°C/km) is expected to occur in the subcrustal mantle of the study region, even taking into account the significant effect of anelasticity that increases the temperature derivative of seismic wave velocities markedly (~2% per 100°C for S wave velocity) [*Goes et al.*, 2000; *Karato*, 1993]. The required thermal gradient, however, is unreasonably high compared with the typical thermal gradient at the base of the lithosphere (2–5°C/km), even much higher than the generous upper bound of 10°C/km at the LAB [*Rychert et al.*, 2005; *Zaranek et al.*, 2004; *Deng et al.*, 2004]. This indicates that temperature variation alone is insufficient to fully account for the observed sharp change of seismic property at the base of the lithosphere in the Tanlu Fault Zone area.

[33] Second, a change in phase, such as partial melting, dehydration, clinoenstatite to orthoenstatite, or basalt to eclogite, etc., may cause abrupt changes in strength and seismic velocity in the upper mantle [*Anderson*, 1995; *Karato and Jung*, 1998; *Hammond and Humphreys*, 2000; *Goes et al.*, 2000; *Hacker et al.*, 2003]. Many phase changes proposed, for example, the transformation from low clinoenstatite to orthoenstatite, might not have widely taken place at ~70 km in eastern China, since their ~600° reaction temperature [*Anderson*, 1995] is apparently much lower than the upper mantle temperature of >1100° at that depth [*Xu et al.*, 1995; *Xu*, 2001]. Basalt to eclogite transformation would increase rather than decrease the seismic velocity, thus cannot be the cause of the velocity drop at the LAB. The presence of a small amount of water or partial melt, on the other hand, could contribute to the upper mantle low-velocity anomalies in both oceanic [e.g., *Karato and Jung*, 1998; *Gaherty et al.*, 1999] and continental regions [e.g., *Rychert et al.*, 2005; *Humphreys and Dueker*, 1994]. Hydration is assumed to reduce velocity primarily by enhancing attenuation [*Karato and Jung*, 1998]. On the basis of the values of shear wave Q (inverse attenuation) derived from seismic tomography for the lithosphere (~250) and the asthenosphere (~50) around the LAB in eastern China [*Li et al.*, 2000; *Hong et al.*, 2003], we estimate the effect of hydration on velocity to be 1.5–5% using the same relationship adopted by *Rychert et al.* [2005]. Thus the shear wave velocity drop due to a dehydration front at the LAB overlaps the estimated velocity contrasts but seems not attain the maximum value of ~7% beneath the Tanlu Fault Zone. Alternatively, 1–2% partial melts present in the asthenosphere may also cause large velocity reductions [*Hammond and Humphreys*, 2000; *Kreutzmann et al.*, 2004] that match our data. In both cases, it requires a hydrated asthenospheric mantle underlying a relatively dehydrated continental lithosphere [*Karato and Jung*, 1998].

[34] Third, compositional variation may also contribute to the difference of seismic velocity. Although it is generally considered to have relatively small effect on upper mantle velocity compared with temperature [*Forte and Perry*, 2000; *Röhm et al.*, 2000], compositional change could become nonignorable and account for as much as ~35% of the difference in S wave velocity (or 1–2% S wave velocity variation) between Archean and tectonic regions [*Goes et al.*, 2000; *Godey et al.*, 2004]. If the present-day thin lithospheric mantle beneath the Tanlu Fault Zone represents a veneer of the Archean cratonic lithosphere that survived the late Mesozoic-Cenozoic tectonic reactivation and thinning, then the sharp seismic velocity gradient at the LAB would be partially attributable to the composition contrast between the cold, refractory lithospheric remnant and the uplifted hot, fertile asthenosphere. Considering the dry nature of the cratonic lithosphere [*Hirth et al.*, 2000] and the unlikeness of rehydrating the remnant mantle veneer over a period of <150 Ma [*Hirth and Kohlstedt*, 1996], this scenario is not in conflict with the hydration or partial melting interpretation mentioned before.

[35] Our analysis indicates that besides a high-temperature gradient, the presence of melt or volatiles in the asthenosphere and compositional contrast between the depleted and dehydrated ancient lithosphere and fertile and hydrated asthenosphere could contribute to the observed strong, sharp LAB of the study region. Thus the observed LAB cannot be defined solely by temperature, but would be representative of a compositional boundary and reflect a rapid rheological change due to the great effect of melt or hydration on viscosity [*Hirth and Kohlstedt*, 1996], analogous to that beneath eastern North America [*Rychert et al.*, 2005]. The preservation of a cratonic lithospheric mantle veneer beneath the Tanlu Fault Zone area, if corroborated by further study, would have profound implications for our understanding of the lithospheric reactivation and thinning in the eastern China continent during late Mesozoic and Cenozoic time.

6. Conclusions

[36] By applying the wave equation based poststack migration method for receiver function imaging to the large

amount of high-quality teleseismic data collected at the broadband seismic stations in eastern China, the lithospheric structure beneath the Tanlu Fault Zone area is well imaged. Our receiver function image and synthetic modeling results suggest that:

[37] 1. The present-day lithosphere of the study region (60–80 km thick) is significantly thinner than its Archean-to-Paleozoic counterpart (>180 km) and display substantial lateral heterogeneities. The LAB exhibits an arc-like geometry with a lateral depth variation of ~20 km within the ~300-km-wide region. The apex of the LAB is roughly coincident with the transverse location of the Tanlu Fault Zone at the surface. The Moho shows small-scale undulations around its average depth of 34 km with a distinct uplift from ~36 km to ~32 km occurred just beneath the Tanlu Fault Zone.

[38] 2. The coincidence of the imaged Moho uplift and the LAB apex with the surface location of the Tanlu Fault Zone confirms the deep penetration of this fault zone, and indicates that it might have acted as a major channel for anthenosphere upwelling accompanying the Mesozoic-Cenozoic continental extension and lithospheric thinning in eastern China.

[39] 3. Both the Moho and the LAB are sharp and strong. The LAB is constrained to have a 3–7% S wave velocity drop over a depth range of 10 km or less.

[40] 4. The rapid seismic velocity drop at the LAB beneath the Tanlu Fault Zone area may be attributed to volatiles or melt in the asthenosphere and possible composition contrast between the preserved cratonic lithospheric veneer and uplifted asthenospheric materials, in conjunction with the temperature effect.

[41] **Acknowledgments.** We thank the Seismic Array Probe Laboratory, IGGCAS, for providing the waveform data and Geoffrey A. Abers, Hersh Gilbert, and an anonymous reviewer for valuable comments and constructive criticism. We are especially grateful to Lianxing Wen for providing his 2-D P-SV hybrid code and thoughtful suggestions. We appreciate the helpful discussions with Qingchen Wang, Fuyuan Wu, and Yigang Xu on interpretation of our results. This research is supported by the National Science Foundation of China (grants 40434012 and 40374015), the National Development and Reform Commission of China (grant 2004-1138), and the Chinese Academy of Sciences.

References

Anderson, D. L. (1990), Geophysics of the continental mantle—An historical perspective, in *Continental Mantle*, edited by M. Menzies, pp. 1–30, Clarendon Press, Oxford, U.K.

Anderson, D. L. (1995), Lithosphere, asthenosphere, and perisphere, *Rev. Geophys.*, *33*, 125–149.

Baumont, D., A. Paul, G. Zandt, S. L. Beck, and H. Pedersen (2002), Lithospheric structure of the central Andes based on surface wave dispersion, *J. Geophys. Res.*, *107*(B12), 2371, doi:10.1029/2001JB000345.

Bostock, M. G. (1997), Anisotropic upper-mantle stratigraphy and architecture of the Slave craton, *Nature*, *390*, 392–395.

Bostock, M. G. (1999), Seismic waves converted from velocity gradient anomalies in the Earth's upper mantle, *Geophys. J. Int.*, *138*, 747–756.

Chen, G. Y., Z. H. Song, C. Q. An, L. H. Cheng, Z. Zhuang, Z. W. Fu, Z. L. Lu, and J. F. Hu (1991), Three dimensional crust and upper mantle structure of the North China region (in Chinese with English abstract), *Acta Geophys. Sin.*, *34*, 172–181.

Chen, L., L. Wen, and T. Zheng (2005a), A wave equation migration method for receiver function imaging: 1. Theory, *J. Geophys. Res.*, *110*, B11309, doi:10.1029/2005JB003665.

Chen, L., L. Wen, and T. Zheng (2005b), A wave equation migration method for receiver function imaging: 2. Application to the Japan subduction zone, *J. Geophys. Res.*, *110*, B11310, doi:10.1029/2005JB003666.

Debayle, E., and B. L. N. Kennett (2000), Anisotropy in the Australasian upper mantle from Love and Rayleigh waveform inversion, *Earth Planet. Sci. Lett.*, *184*, 339–351.

Deschamps, F., J. Trampert, and R. Snieder (2002), Anomalies of temperature and iron in the uppermost mantle inferred from gravity data and tomographic models, *Phys. Earth Planet. Inter.*, *129*, 245–264.

Deng, J. (1988), Continental rift-related magmatism and deep processes, in *The Study of Cenozoic Basalts and the Upper Mantle beneath Eastern China (Attachment: Kimberlites)* (in Chinese), edited by J. S. Chi, pp. 201–218, China Univ. of Geosci. Press, Wuhan, China.

Deng, J., H. Zhao, Z. Luo, Z. Guo, and X. Mo (1998), Mantle plumes and lithosphere motion in east Asia, in *Mantle Dynamics and Plate Interactions in East Asia*, *Geodyn. Ser.*, vol. 27, edited by M. F. J. Flower et al., pp. 59–66, AGU, Washington, D. C.

Deng, J., X. Mo, H. Zhao, Z. Wu, Z. Luo, and S. Su (2004), A new model for the dynamic evolution of Chinese lithosphere: "Continental roots-plume tectonics", *Earth Sci. Rev.*, *65*, 223–275.

Duffy, T. S., and D. L. Anderson (1989), Seismic wave speeds in mantle minerals and the mineralogy of the upper mantle, *J. Geophys. Res.*, *94*, 1895–1912.

Dziewonski, A., and D. L. Anderson (1981), Preliminary reference Earth model, *Phys. Earth Planet. Inter.*, *25*, 297–356.

Fan, W. M., and M. A. Menzies (1992), Destruction of aged lower lithosphere and accretion of asthenosphere mantle beneath eastern China, *Geotect. Metall.*, *16*, 171–180.

Fan, W. M., H. F. Zhang, J. Baker, K. E. Jarvis, P. R. D. Mason, and M. A. Menzies (2000), On and off the North China Craton: Where is the Archaean keel?, *J. Petrol.*, *41*, 933–950.

Farra, V., and L. Vinnik (2000), Upper mantle stratification by P and S receiver functions, *Geophys. J. Int.*, *141*, 699–712.

Forte, A. M., and H. K. C. Perry (2000), Geodynamic evidence for a chemically depleted continental tectosphere, *Science*, *290*, 1940–1944.

Gaherty, J. B., M. Kato, and T. H. Jordan (1999), Seismological structure of the upper mantle: A regional comparison of seismic layering, *Phys. Earth Planet. Inter.*, *110*, 21–41.

Gao, S., B. R. Zhang, Z. M. Jin, H. Kern, T. C. Luo, and Z. D. Zhao (1998), How mafic is the lower continental crust?, *Earth Planet. Sci. Lett.*, *161*, 101–117.

Gao, S., R. L. Rudnick, and H. L. Yuan (2004), Recycling lower continental crust in the North China craton, *Nature*, *432*, 892–897.

Godey, S., F. Deschamps, J. Trampert, and R. Snieder (2004), Thermal and compositional anomalies beneath the North American continent, *J. Geophys. Res.*, *109*, B01308, doi:10.1029/2002JB002263.

Goes, S., R. Govers, and P. Vacher (2000), Shallow mantle temperatures under Europe from P and S wave tomography, *J. Geophys. Res.*, *105*, 11,153–11,169.

Griffin, W. L., A. Zhang, S. Y. O'Reilly, and C. G. Ryan (1998), Phanerozoic evolution of the lithosphere beneath the Sino-Korean craton, in *Mantle Dynamics and Plate Interactions in East Asia*, *Geodyn. Ser.*, vol. 27, edited by M. F. J. Flower et al., pp. 107–126, AGU, Washington, D. C.

Hacker, B. R., G. A. Abers, and S. M. Peacock (2003), Subduction factory: 1. Theoretical mineralogy, density, seismic wave speeds, and H_2O content, *J. Geophys. Res.*, *108*(B1), 2029, doi:10.1029/2001JB001127.

Hammond, W. C., and E. D. Humphreys (2000), Upper mantle seismic wave velocity: Effects of realistic partial melt geometries, *J. Geophys. Res.*, *105*, 10,975–10,986.

Hirth, G., and D. L. Kohlstedt (1996), Water in the oceanic upper mantle; implications for rheology, melt extraction and the evolution of the lithosphere, *Earth Planet. Sci. Lett.*, *144*, 93–108.

Hirth, G., R. L. Evans, and A. D. Chave (2000), Comparison of continental and oceanic mantle electrical conductivity: Is the Archean lithosphere dry?, *Geochem. Geophys. Geosyst.*, *1*(12), doi:10.1029/2000GC000048.

Hong, X., J. Zhu, J. Cao, and Z. Xu (2003), Tomography of the 3-D S-wave quality factor of the crust and upper mantle in China (in Chinese with English abstract), *Chin. J. Geophys.*, *46*(5), 642–651.

Hu, S., L. He, and J. Wang (2000), Heat flow in the continental area of China: A new data set, *Earth Planet. Sci. Lett.*, *179*, 407–419.

Humphreys, E. D., and K. G. Dueker (1994), Physical state of the western U.S. upper mantle, *J. Geophys. Res.*, *99*, 9635–9650.

Huang, Z., W. Su, Y. Peng, Y. Zheng, and H. Li (2003), Rayleigh wave tomography of China and adjacent regions, *J. Geophys. Res.*, *108*(B2), 2073, doi:10.1029/2001JB001696.

Jahn, B. M., B. Auvray, J. Comichet, Y. L. Bai, Q. H. Shen, and D. Y. Liu (1987), 3.5 Ga old amphibolites from eastern Hebei province China: Field occurrence, petrography, Sm-Nd isochron age and REE geochemistry, *Precambrian Res.*, *34*, 311–346.

Karato, S.-I. (1993), Importance of anelasticity in the interpretation of seismic tomography, *Geophys. Res. Lett.*, *20*, 1623–1626.

Karato, S.-I., and H. Jung (1998), Water, partial melting and the origin of the seismic low velocity and high attenuation zone in the upper mantle, *Earth Planet. Sci. Lett.*, *157*, 193–207.

Kennett, B. L. N., and E. R. Engdahl (1991), Travel times for global earthquake location and phase identification, *Geophys. J. Int.*, *105*, 429–465.

Kreutzmann, A., et al. (2004), Temperature and melting of a ridge-centred plume with application to Iceland. part II: Predictions for electromagnetic and seismic observables, *Geophys. J. Int.*, *159*, 1097–1111.

Kumar, P., X. Yuan, R. Kind, and G. Kosarev (2005), The lithosphere-asthenosphere boundary in the Tien Shan-Karakoram region from S receiver functions: Evidence for continental subduction, *Geophys. Res. Lett.*, *32*, L07305, doi:10.1029/2004GL022291.

Langston, C. A. (1977), The effect of planar dipping structure on source and receiver responses for constant ray parameter, *Bull. Seismol. Soc. Am.*, *67*, 1029–1050.

Li, G., G. Xu, E. Gao, and Y. Xu (2000), Tomography for 3-D transverse wave quality factor of crust and upper mantle in east China (in Chinese), *Acta Seismol. Sin.*, *22*(1), 73–81.

Li, X., R. Kind, X. Yuan, I. Wölbern, and W. Hanka (2004), Rejuvenation of the lithosphere by the Hawaiian plume, *Nature*, *427*, 827–829.

Liu, D., A. P. Nutman, W. Compston, J. Wu, and Q. She (1992), Remnants of >3800 Ma crust in the Chinese part of the Sino-Korean craton, *Geology*, *20*, 339–342.

Liu, R. (Ed.) (1992), *The Age and Geochemistry of Cenozoic Volcanic Rock in China*, 427 pp., Seismol. Press, Beijing.

Ma, X., C. Liu, and G. Liu (1991), *Global Geoscience Transect 2: Xiangshui to Mandal Transect, North China*, AGU, Washington, D. C.

Menzies, M. A., W. Fan, and Z. Ming (1993), Palaeozoic and Cenozoic lithoprobes and loss of >120 km of Archaean lithosphere, Sino-Korean craton, China, in *Magmatic Processes and Plate Tectonics*, edited by H. M. Prichard et al., *Geol. Soc. Spec. Publ.*, *76*, 71–81.

Montelli, R., G. Nolet, F. A. Dahlen, G. Masters, E. R. Engdahl, and S.-H. Hung (2004), Finite-frequency tomography reveals a variety of plumes in the mantle, *Science*, *303*, 338–343.

Owens, T. J., S. R. Taylor, and G. Zandt (1987), Crustal structure at regional test network stations determined from inversion of broadband teleseismic P waveforms, *Bull. Seismol. Soc. Am.*, *77*, 631–662.

Polet, J., and D. L. Anderson (1995), Depth extent of cratons as inferred from tomographic studies, *Geology*, *23*(3), 205–208.

Poppeliers, C., and G. L. Pavlis (2003a), Three-dimensional, prestack, plane wave migration of teleseismic P-to-S converted phases: 1. Theory, *J. Geophys. Res.*, *108*(B2), 2112, doi:10.1029/2001JB000216.

Poppeliers, C., and G. L. Pavlis (2003b), Three-dimensional, prestack, plane wave migration of teleseismic P-to-S converted phases: 2. Stacking multiple events, *J. Geophys. Res.*, *108*(B5), 2267, doi:10.1029/2001JB001583.

Ren, J., et al. (2002), Late Mesozoic and Cenozoic rifting and its dynamic setting in eastern China and adjacent areas, *Tectonophysics*, *344*, 175–205.

Röhm, A. H. E., R. Snieder, S. Goes, and J. Trampert (2000), Thermal structure of continental upper mantle inferred from S-wave velocity and surface heat flow, *Earth Planet. Sci. Lett.*, *181*, 395–407.

Ryberg, T., and M. Weber (2000), Receiver function arrays: A reflection seismic approach, *Geophys. J. Int.*, *141*, 1–11.

Rychert, C. A., K. M. Fischer, and S. Rondenay (2005), A sharp lithosphere-asthenosphere boundary imaged beneath eastern North America, *Nature*, *436*, 542–545.

Sheehan, A. F., P. M. Shearer, H. J. Gilbert, and K. G. Dueker (2000), Seismic migration processing of P-SV converted phases for mantle discontinuity structure beneath the Snake River Plain, western United States, *J. Geophys. Res.*, *105*, 19,055–19,065.

Tian, X., Q. Wu, Z. Zhang, J. Teng, and R. Zeng (2005), Identification of multiple reflected phases from migration receiver function profile: An example for the INDEPTH-III passive teleseismic P waveform data, *Geophys. Res. Lett.*, *32*, L08301, doi:10.1029/2004GL021885.

Tian, Z., P. Han, and K. Xu (1992), The Mesozoic-Cenozoic east China rift system, *Tectonophysics*, *208*, 341–363.

van der Lee, S. (2002), High-resolution estimates of lithospheric thickness from Missouri to Massachusetts, USA, *Earth Planet. Sci. Lett.*, *203*, 15–23.

van der Meijde, M., F. Marone, D. Giardini, and S. van der Lee (2003), Seismic evidence for water deep in Earth's upper mantle, *Science*, *300*, 1556–1558.

Vinnik, L., and V. Farra (2000), Upper mantle stratification by P and S receiver functions, *Geophys. J. Int.*, *141*, 699–712.

Wang, X. F., et al. (Eds.) (2000), *The Tanlu Fault Zone*, 82 pp., Geol. Press, Beijing.

Wen, L., and D. V. Helmberger (1998), A two-dimensional P-SV hybrid method and its application to modeling localized structures near the core-mantle boundary, *J. Geophys. Res.*, *103*, 17,901–17,918.

Woodhouse, J. H., and T. Trampert (1995), Global upper mantle structure inferred from surface wave and body wave data, *Eos Trans. AGU*, *76*(46), Fall Meet. Suppl., F422.

Wu, Q., and R. Zeng (1998), The crustal structure of Qinghai-Xizang plateau inferred from broadband teleseismic waveform (in Chinese with English abstract), *Chin. J. Geophys.*, *41*, 669–679.

Xu, Y. G. (1999), Roles of thermo-mechanic and chemical erosion in continental lithospheric thinning (in Chinese with English abstract), *Bull. Mineral. Petrol. Geochem.*, *18*, 1–5.

Xu, Y. G. (2001), Thermotectonic destruction of the Archean lithospheric keel beneath eastern China: Evidence, timing, and mechanism, *Phys. Chem. Earth A*, *26*, 747–757.

Xu, Y. G., C. Y. Lin, L. B. Shi, J.-C. Mercie, and J. V. Ross (1995), Upper mantle geotherm for eastern China and its geological implications (in Chinese), *Sci. China, Ser. B*, *38*, 1482–1492.

Xu, Y. G., S. L. Chung, J. L. Ma, and L. B. Shi (2004), Contrasting Cenozoic lithospheric evolution and architecture in the eastern and western Sino-Korean craton: Constraints from geochemistry of basalts and mantle xenoliths, *J. Geol.*, *112*, 593–605.

Yuan, X. C. (1996), Velocity structure of the Qiling lithosphere and mushroom cloud model (in Chinese), *Sci. China, Ser. D*, *39*, 233–244.

Zaranek, S. E., E. M. Parmentier, and K. M. Fischer (2004), Effects of basal drag and ablation on the evolution of cratonic lithosphere, *Eos Trans. AGU*, *85*(17), Jt. Assem. Suppl., Abstract T41C-03.

Zhang, B. X., and Y. A. Tang (1988), Crustal structure of the Qishu fault zone (in Chinese), *Earthquake Res. China*, *4*(3), 16–22.

Zhang, H., and M. Sun (2002), Geochemistry of Mesozoic basalts and mafic dikes in southeastern North China craton, and tectonic implication, *Int. Geol. Rev.*, *44*, 370–382.

Zhao, D., A. Hasegawa, and H. Kanamori (1994), Deep structure of Japan subduction zone as derived from local, regional, and teleseismic events, *J. Geophys. Res.*, *99*, 22,313–22,329.

Zhao, D., T. Matsuzawa, and A. Hasegawa (1997), Morphology of the subducting slab boundary in the northeastern Japan arc, *Phys. Earth Planet. Inter.*, *102*, 89–104.

Zheng, J., S. Y. O'Reilly, W. L. Griffin, F. Lu, and M. Zhang (1998), Nature and evolution of Cenozoic lithospheric mantle beneath Shandong peninsula, Sino–Korean craton, *Int. Geol. Rev.*, *40*, 471–499.

Zheng, J., S. Y. O'Reilly, W. L. Griffin, F. Lu, M. Zhang, and N. J. Pearson (2001), Relict refractory mantle beneath the eastern North China block: Significance for lithosphere evolution, *Lithos*, *57*, 43–66.

Zheng, T., L. Zhao, and L. Chen (2005), A detailed receiver function image of the sedimentary structure in the Bohai Bay Basin, *Phys. Earth Planet. Inter.*, *152*, 129–143.

Zhu, J., J. Cao, X. Cai, Z. Yan, and X. Cao (2002), High resolution surface wave tomography in east Asia and west Pacific marginal seas (in Chinese with English abstract), *Chin. Geophys, J.*, *45*(5), 646–664.

Zhu, L. (2000), Crustal structure across the San Andreas Fault, southern California from teleseismic converted waves, *Earth Planet. Sci. Lett.*, *179*, 183–190.

L. Chen, W. Xu, and T. Zheng, Seismological Laboratory (SKL-LE), Institute of Geology and Geophysics, Chinese Academy of Sciences, Beijing 100029, China. (lchen@mail.iggcas.ac.cn)